Miniaturized Monolithic 3-D Printed Bandpass Filters Using Nested Spherical Resonators

Jiawei Liu, *Member, IEEE*, Kunchen Zhao, *Graduate Student Member, IEEE*, and Dimitra Psychogiou, *Senior Member, IEEE*

***Abstract*— This article reports on a new class of highly miniaturized nested spherical bandpass filters (BPFs) alongside a monolithic integration concept. Miniaturization is achieved by a nested spherical resonator approach, i.e., by incorporating a postsupported sphere within the volume of a hollow spherical resonator. In this manner, the resonant frequencies of the first four modes are lowered when compared to conventional unloaded spherical resonators, allowing for smaller BPFs to be materialized. Alternative BPF topologies using the fundamental mode as well as a combination of higher order modes are considered to further miniaturize the filter volume. Scalability to higher order transfer functions through cascaded configurations of multimode resonators is explored. Monolithic integration is enabled by digital additive manufacturing (AM) techniques using stereolithography apparatus (SLA). For proof-of-concept validation purposes three prototypes were designed, manufactured, and tested. They include: 1) a two-pole BPF with a passband centered at 2.72 GHz, fractional bandwidth (FBW) of 33.1%, and minimum in-band insertion loss (IL) of 0.15 dB; 2) a three-pole BPF with a passband centered at 6.94 GHz, FBW of 13.65% and minimum in-band IL of 0.07 dB; and 3) a six-pole BPF with a passband centered at 6.88 GHz, FBW of 12.77% and minimum in-band IL of 0.3 dB.**

***Index Terms*— 3-D printing, additive manufacturing (AM), bandpass filters (BPFs), spherical resonator, stereolithography apparatus (SLA).**

I. Introduction

MODERN wireless communication systems are increasingly becoming more complex due to the need to support multiple applications with diverse spectral and power requirements. Higher operational frequencies, higher data rates, and improved spectral and power efficiency are other challenging requirements that these systems need to fulfill. To facilitate operation in interference-dominated environments, RF filters with high unloaded quality-factor (Q) need to be incorporated in their RF transceivers of these systems to acquire the desired bands of interest with the minimum possible loss penalty while suppressing the unwanted interference. Low-weight and small form factor are other important considerations that need to be considered for their RF design.

Three-dimensional resonators using rectangular [1], [2], spherical [3], cylindrical cavities [4], or dielectric-loaded cavity resonators [5] have been extensively investigated for the realization of low loss and highly performing RF filters. Compared to their planar transmission counterparts, such as microstrip, coplanar waveguide, and substrate integrated waveguide (SIW) technologies, they exhibit significantly higher Q (up to 10×) and can handle high levels of RF power (>50 dBm) [6], [7], [8]. However, they are large in size, particularly, when designed for low frequencies of operation. Capacitively-loaded coaxial cavity resonator bandpass filters (BPFs) [9], [10] or ridge-waveguide BPFs [11], [12] have recently been proposed as miniaturization alternatives for 3-D RF filtering at the expense of Q and in-band insertion loss (IL). In yet another approach, multimode resonators are used within the filter volume to miniaturize their size by adding poles or transmission zeros (TZs) in the filtering transfer function without needing to cascade additional resonators. Notable demonstrations of this approach include a waveguide dual mode filter [13] using transverse magnetic and nonresonating modes, a multimode waveguide filter [14] using the epsilon-near-zero (ENZ) channel, a waveguide filter using the parallel multimode spherical cavity [15] and a BPF [16] using high-Q quadruple-mode rectangular waveguide resonators. However, all of the aforementioned configurations are expensive and bulky. Furthermore, they need to be manufactured as split-blocks and assembled through screws requiring postfabrication tuning.

Additive manufacturing (AM) techniques (or 3-D printing) such as fused deposition modeling (FDM) [17], stereolithography apparatus (SLA) [10], digital light processing (DLP) [18], direct metal laser sintering (DMLS) [19], selective laser melting (SLM) [20], and electron beam melting (EBM) [21], have been increasingly used for the manufacturing of 3-D RF filters [22], [23], [24], [25], [26], [27], antennas [28], [29], [30], [31] and RF couplers [32], [33], [34]. They have the potential to reduce the weight of RF components

Manuscript received 3 March 2023; revised 12 May 2023; accepted 24 July 2023. Date of publication 21 August 2023; date of current version 18 October 2023. This work was supported in part by the Science Foundation Ireland (SFI) under Grant 20/RP/8334 and the China Scholarship Council (CSC). Recommended for publication by Associate Editor S. Roy upon evaluation of reviewers' comments. *(Corresponding author: Jiawei Liu.)*

Jiawei Liu was with the Tyndall National Institute, Cork T12, R5CP Ireland. He is now with the School of Electronic Science and Engineering, University of Electronic Science and Technology of China, Chengdu 611731, China (e-mail: liujwgyem@std.uestc.edu.cn).

Kunchen Zhao is with the Department of Electrical, Computer and Energy Engineering, University of Colorado Boulder, Boulder, CO 80309 USA (e-mail: Kunchen.Zhao@colorado.edu).

Dimitra Psychogiou is with the School of Engineering, University College Cork, Cork T12, K8AF Ireland, and also with the Tyndall National Institute, Cork T12, R5CP Ireland (e-mail: dpsychogiou@ucc.ie).

Color versions of one or more figures in this article are available at https://doi.org/10.1109/TCPMT.2023.3306772.

Digital Object Identifier 10.1109/TCPMT.2023.3306772

and the design-to-prototyping cycle. Furthermore, they allow for complex geometries to be realized that cannot be manufactured with conventional CNC machining techniques. However, most of the 3-D printed RF components that have been presented to date are based on plastic-/resin-based AM techniques (e.g., FDM, SLA, and DLP). They are manufactured as split blocks and are assembled using screws [35], [36], [37] due to the need for internal metallization. As such, they end up being really large and heavy and suffer from radiation losses. Metal-based AM techniques (e.g., DMLS, SLM, and EBM) allow for monolithic integration [38]; however, the RF components exhibit high surface roughness which results in high levels of in-band IL [39], [40].

Plastic-/resin-based monolithic integration approaches using SLA AM have been recently proposed for the realization of open-ended RF components such as the ones using rectangular waveguides [41] and spherical resonators [42], [43], [44]. Monolithic SLA-based integration concepts were also recently demonstrated for fully enclosed coaxial-resonator based configurations such as single- and multiband BPFs and diplexers [9], [25], [45] with high levels of complexity. However, most of the SLA-based fully enclosed passive RF components still need to be divided into several parts to allow for internal metallization, and as such they are manufactured as split blocks and are assembled with screws or other fixtures. For example, in [46], a split-block SLA-based coaxial filter using SIR resonators is demonstrated with an IL of 1.1 dB whereas in [47], a SLA-based split-block four-pole filter using conical resonators is presented. In the plastic-/resin-based SLA AM filter in [45] slots were added to facilitate metallization of its internal walls [45].

In this article, new types of RF filters using novel single-mode and multimode metal nested spherical resonator configurations are investigated for the first time for the realization of high-Q and highly miniaturized 3-D filters. The center frequencies of filters were chosen close to the ones of applications within the FR1 band, i.e., sub-6 GHz. The proposed concept is based on the incorporation of a postsupported fully metallic sphere within a hollow sphere. In this manner, the resonant frequencies of the first four resonant modes are significantly lowered when compared to a conventional hollow spherical resonator having the same outer dimensions. Further miniaturization is achieved by exploiting multiple resonant modes within a single resonator to create high-order filtering transfer functions.

This article is organized as follows. Section II introduces the theoretical foundations of the proposed nested spherical resonator concept alongside its application to the realization of compact and high-order RF filters. In Section III, practical design and integration aspects are discussed through the design, manufacturing, and testing of three BPF prototypes. Finally, the major contributions of this work are outlined in Section IV.

II. Design and Analysis of the Filters

A. Nested Spherical Resonator Concept

The geometrical details of the proposed nested spherical resonator concept are shown in Fig. 1(a). It is composed of a spherical cavity that is loaded by a postsupported metallic sphere. The resonator loading makes the resonant frequencies of the four first resonant modes to be lower than a conventional unloaded spherical resonator allowing for smaller RF filters to be realized. To get a better insight on the resonant capabilities of the proposed resonator concept, eigenmode simulation analysis is performed in ANSYS HFSS for the first four resonant modes whose electric field distribution is provided in Fig. 1(b). As noticed, the second and the third modes are degenerate and can be used for compact BPF design. To demonstrate the size-compactness merits of the proposed resonator concept, Fig. 2 provides a comparison of the resonant frequencies of the first four modes of a conventional hollow spherical resonator and the proposed nested spherical resonator. Evidently, the nested spherical resonator resonates at lower frequencies than those of a conventional hollow spherical resonator with the same dimensions.

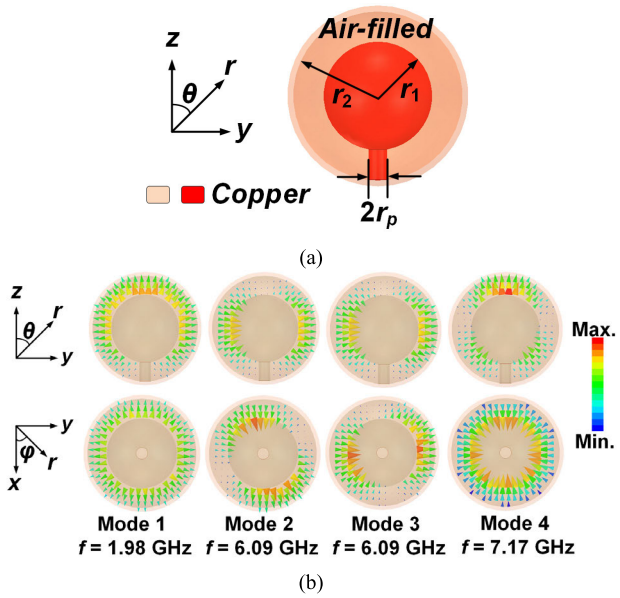

Fig. 1. (a) 3-D geometry of the nested-spherical resonator and (b) E-field distribution of the first four resonant modes. The geometrical parameters of the resonator are: $r_1 = 9$ mm, $r_2 = 14$ mm, and $r_p = 1.5$ mm.

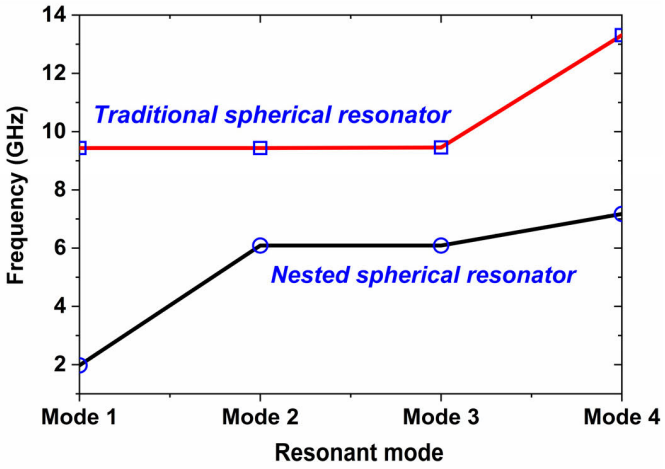

Fig. 2. Resonant frequencies of the first four resonant modes of a conventional hollow spherical resonator and the proposed nested spherical resonator. In both examples, the radius of the outer cavity r_2 is 14 mm.

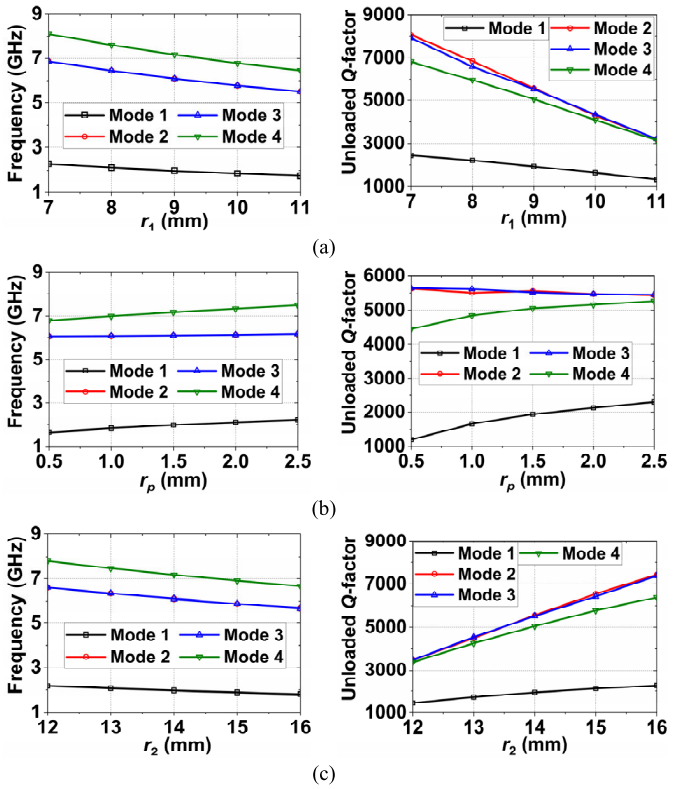

Fig. 3. Resonant frequency and Q of the first four modes of the nested spherical resonator for alternative geometrical parameters: (a) r_1, (b) r_p, and (c) r_2.

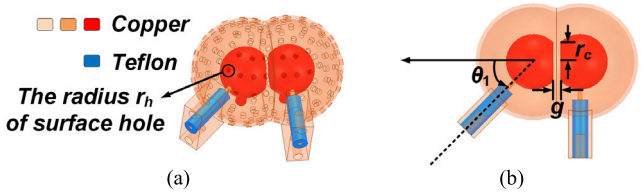

Fig. 4. Geometry of the two-pole BPF using two nested spherical resonators. (a) Side view. (b) Top view.

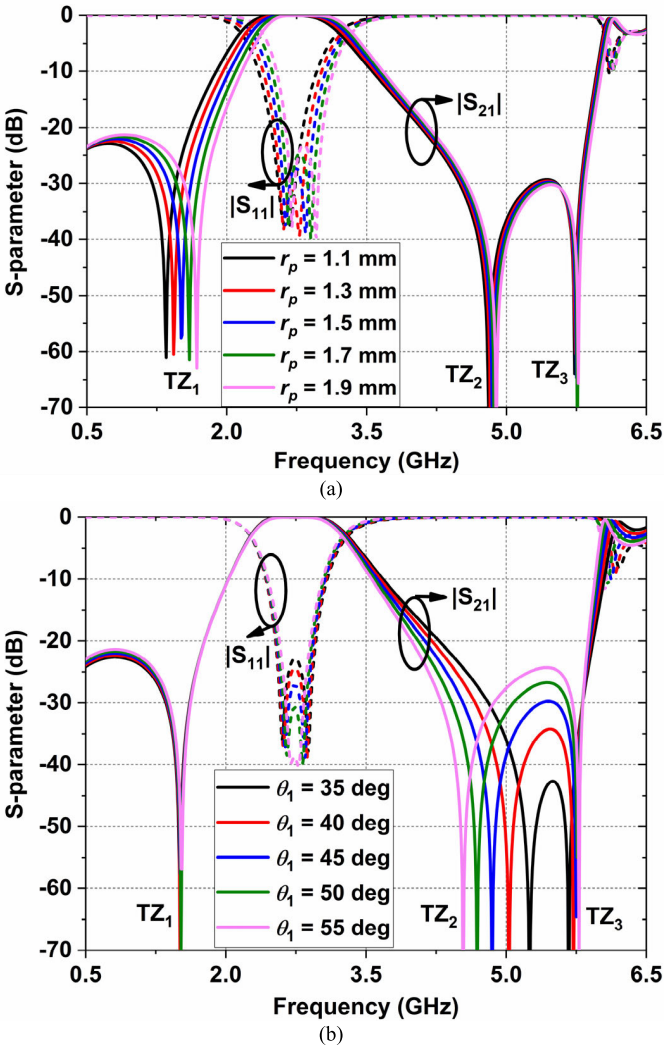

Fig. 5. EM simulated S-parameters of the two-pole BPF in Fig. 4 as a function of different geometrical parameters. (a) r_p. (b) θ_1. The rest of the geometrical parameters are: $r_1 = 7.1$ mm, $r_2 = 14$ mm, $g = 2$ mm, and $r_c = 5.08$ mm.

To further demonstrate the resonant capabilities of the proposed resonator concept, Fig. 3 depicts how the resonant frequency and Q of the first four modes can be controlled by altering the geometrical parameters of the resonator. As shown, in Fig. 3(a), the first four modes and their Q decrease when the radius r_1 of the inner sphere increases. Furthermore, the resonant frequency and Q of the first and the fourth modes increase, while those of the two degenerated modes (second and third modes) remain almost constant when r_p increases as shown in Fig. 3(b). Moreover, the resonant frequency of the four modes decreases while their Q increases with the increase of the radius of the outer spherical cavity r_2, as shown in Fig. 3(c).

To verify the usefulness of the four different modes in the realization of compact and high-performing BPFs, three different filter topologies have been designed and analyzed and are presented in Sections II-B–II-D.

B. Two-Pole BPF Using Two Coupled Resonators

The first BPF topology is based on two coupled nested-spherical resonators as shown in Fig. 4. Its two-pole passband is formed by the fundamental mode (mode 1) of each resonator. Furthermore, three-TZ are present in the out-of-band power transmission response resulting in a two-pole/three-TZ transfer function as shown in Figs. 5–7. The TZs are due to the multiple RF signal paths that are created within the filter due to the presence of the multiple modes. These RF signals destructively add at frequencies where the TZs are present. Figs. 5–7 also show how the poles and the TZs of the transfer function can be controlled by altering different geometrical parameters. Specifically, Fig. 5, demonstrates how the radius r_p of metal post and the rotation angle θ_1 of the input port affect the BPF performance. As shown in Fig. 5(a), larger r_p, makes the two poles and the TZ_1 move to higher frequencies while TZ_2 and TZ_3 remain constant. From Fig. 5(b), it can be seen that the two poles move closer to each other with the increase of θ_1 whereas the TZ_1 and the TZ_3 remain almost constant and the TZ_2 moves closer to the passband. Furthermore, in Fig. 6(a) the effect of r_1 is studied. Specifically, the poles and TZs move to lower frequencies with the increase of r_1. The frequency details of the transmission poles, as r_1 is altered,

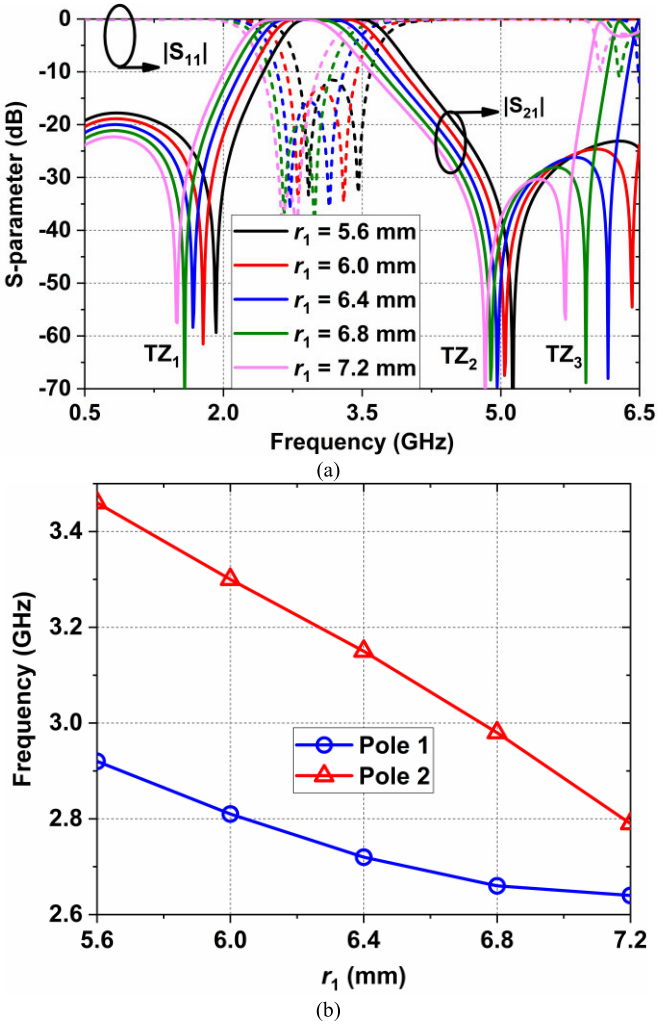

Fig. 6. (a) EM-simulated S-parameters of the two-pole BPF in Fig. 4 as a function of r_1. (b) EM-simulated resonant frequency of the two in-band poles as a function of r_1. In these results, $r_2 = 14$ mm, $r_p = 1.5$ mm, $g = 2$ mm, $r_c = 5.08$ mm, and $\theta_1 = 45°$.

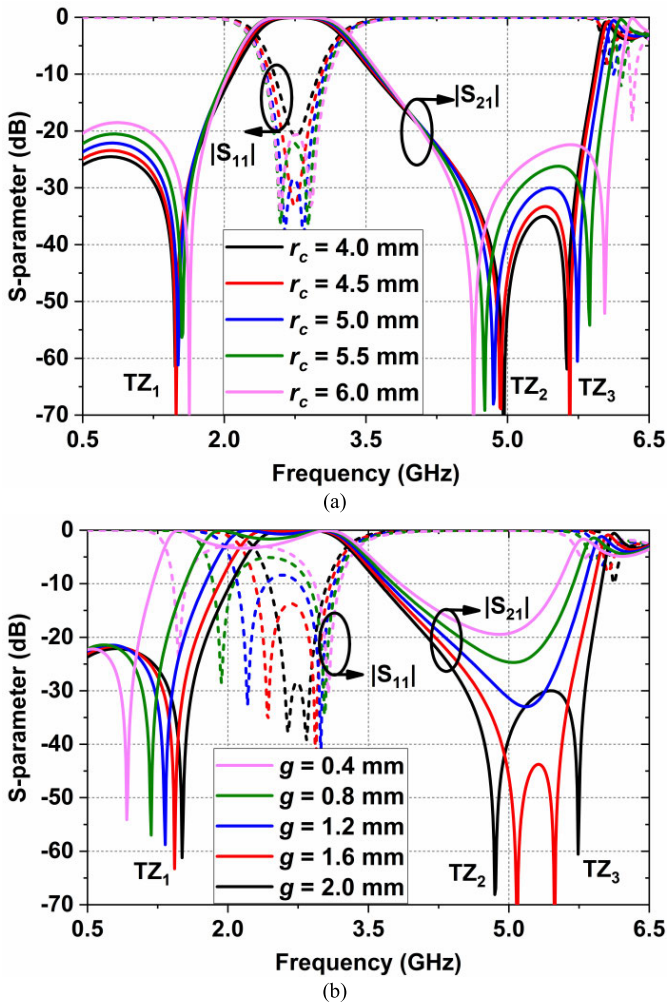

Fig. 7. EM-simulated S-parameters of the two-pole BPF in Fig. 4 as a function of: (a) g. (b) r_c. The rest of the geometrical parameters are: $r_1 = 7.1$ mm, $r_2 = 14$ mm, $r_p = 1.5$ mm, and $\theta_1 = 45°$.

are depicted in Fig. 6(b). To further facilitate control of the passband bandwidth by altering the coupling between the fundamental modes of the two resonators, a part from each of the inner metal spheres is removed as shown in Fig. 4(b).

The filters's performance as a function of the gap g and radius r_c are provided in Fig. 7. As shown, when r_c (i.e., the radius of coupling area between two spheres) increases the in-band return loss (RL) level becomes higher. Moreover, TZ_1 moves to a higher frequency, and TZ_2 and TZ_3 move opposite to each other. When g increases, the passband poles come closer to each other allowing for narrower BW states to be obtained. Furthermore, the TZ_1 moves to higher frequencies, and the TZ_2 and TZ_3 will move opposite to each other when the g increases. According to the above analysis, the bandwidth and positions of the TZs and poles can be adjusted by controlling r_c and g.

Taking into consideration the aforementioned parametric studies, the two-pole BPF transfer function can be designed as follows.

1) Perform eigenmode simulations and determine the dimensions of the nested spherical resonator in Fig. 1 so that the fundamental mode (mode 1) of the resonator resonates at the desired center frequency f_c.

2) Connect two resonators as shown in Fig. 4 and perform a set of parametric studies as shown in Figs. 5–7 to determine the passband BW, TZs, and filter matching levels.

3) Select g and r_c for the desired filter BW to be obtained.

4) Specify the location of the TZs by altering r_p (TZ_1), θ_1 (TZ_2), r_1, r_c, and g (TZ_1, TZ_2, and TZ_3).

5) Through r_c and θ_1 specify the desired RL level.

A design example for a center frequency of 2.77 GHz and fractional BW of 36.1% is shown in Fig. 8. To facilitate metallization of the internal surfaces of the filter after being monolithically manufactured through SLA 3-D printing, nonradiating holes need to be added on its surfaces to allow for the copper platting solution to flow through the filter volume. As such, the location and the size of the holes need to be carefully analyzed by electromagnetic (EM) simulations to ensure that they do not affect the BPF's performance. Fig. 8 shows a comparison of the BPFs S-parameters in the presence or absence of holes as well as for different hole sizes with radius r_h between 0.5 and 0.9 mm. As shown, the presence of the holes has a minimal impact on the RF

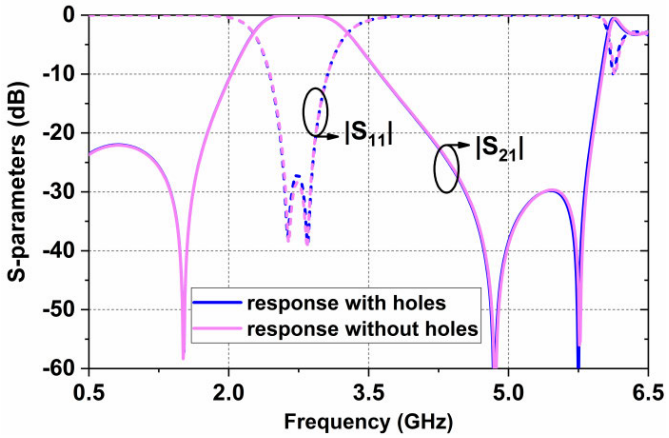

(a)

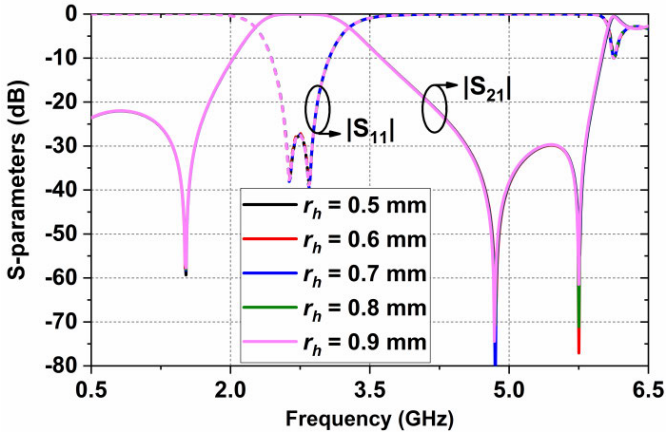

(b)

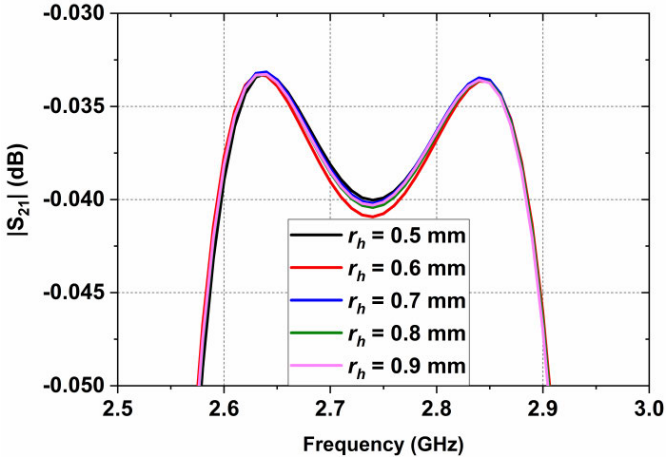

(c)

Fig. 8. EM-simulated response of the two-pole BPF in Fig. 4 in the absence or presence of Cu-platting holes. (a) Filter performance in the absence or presence of holes with a radius $r_h = 0.75$ mm. (b) Broadband filter performance for alternative hole sizes. (c) Passband performance for alternative hole sizes. The rest of the filter dimensions are $r_1 = 7.1$ mm, $r_2 = 14$ mm, $r_p = 1.5$ mm, $g = 2$ mm, $r_c = 5.08$ mm, and $\theta_1 = 45°$.

performance of the filter. For these states, the effective Q remains almost constant and around 1086 in the case of the surface holes with radius $r_h = 0.75$ mm. As such, holes with a radius of 0.75 mm are used for the practical realization of the two-pole BPF as well as the rest of the BPF examples in this article.

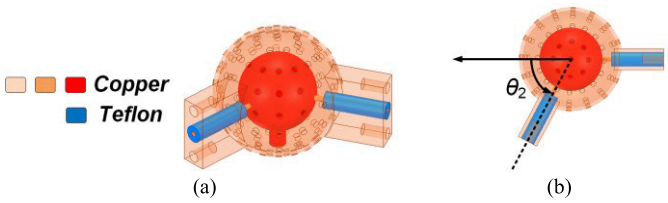

(a) (b)

Fig. 9. Three-pole BPF by coupling modes 2–4 in a single nested spherical resonator. (a) Side view. (b) Top view.

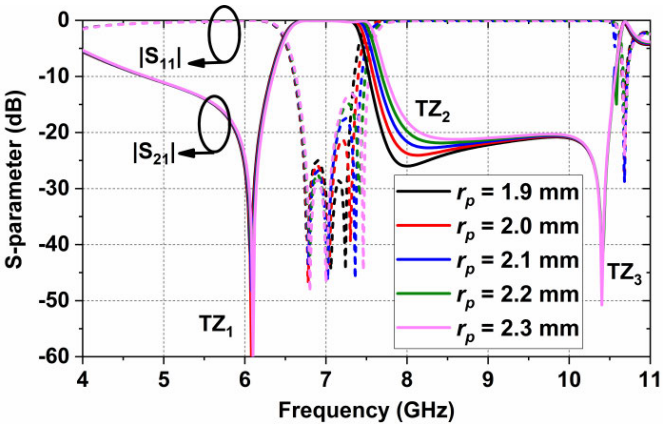

(a)

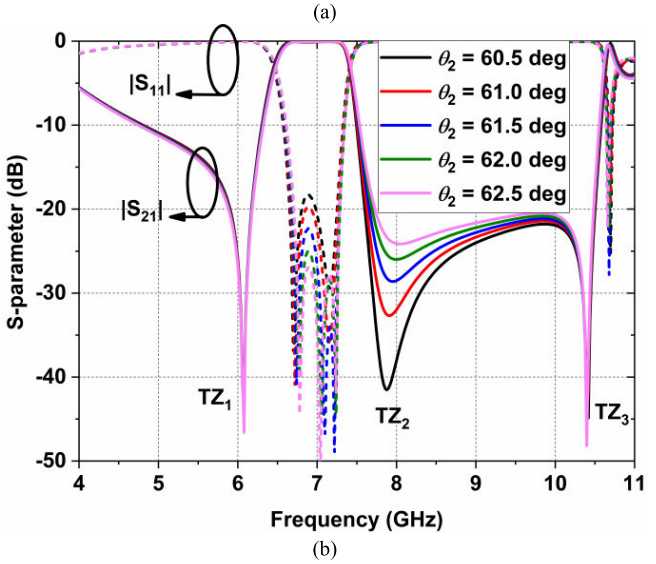

(b)

Fig. 10. EM-simulated S-parameters of the three-pole BPF in Fig. 9 as a function of alternative geometrical parameters. (a) r_p. (b) θ_2. The rest of the geometrical parameters are: $r_1 = 9.1$ mm and $r_2 = 14$ mm.

C. Three-Pole BPF Using a Single Nested Resonator Configuration

The geometrical details of the three-pole BPF using a single nested spherical resonator are depicted in Fig. 9. As shown in Fig. 3(b), the frequencies of the second, third, and forth modes (i.e., mode 2–4) will come close to each other with the decrease of r_p which makes it possible to form passband based on these three modes. Furthermore, three TZs appear in the out-of-band response with the overall transfer function having three-poles and three TZs. To demonstrate the design principles of this filtering configuration, the power transmission and reflection response of the three-pole/three-TZ for alternative geometrical parameters are shown in Fig. 10.

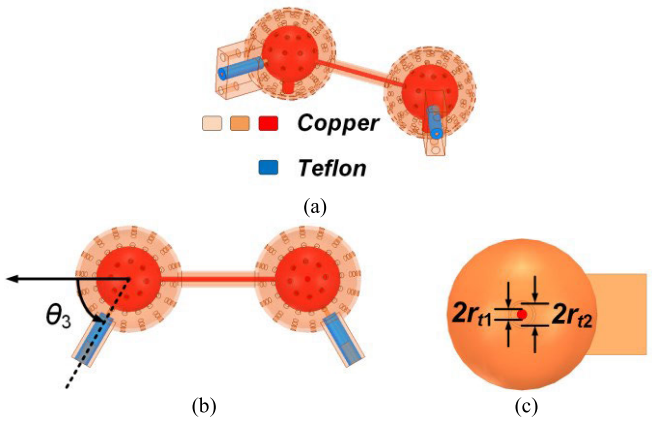

Fig. 11. Six-pole BPF based on two nested spherical resonators. (a) Bird-eye view. (b) Top view ($\theta_3 = 60°$). (c) Side cross section view.

Specifically, Fig. 10(a) shows that when r_p increases, the third pole (mode 4) moves to higher frequencies whereas the frequencies of the rest of the poles remain constant. Besides, the frequency of TZ_1 and TZ_3 remains unaltered, and the stopband isolation at high frequencies worsens with the increase of r_p. In Fig. 10(b), it is shown that the in-band RL can be adjusted by altering θ_2, and the high frequency stopband isolation at high frequencies worsens with the increase of θ_2. On the basis of these results, the bandwidth, RL, and stopband isolation of this filter can be adjusted through r_p and θ_2. Moreover, since this filter and the two-pole BPF use the same resonator, the effect of the inner radius of the metallic sphere r_1 is similar to that of the two-pole BPF. Based on the aforementioned performance trade-offs the BPF transfer function can be designed as follows.

1) Through eigenmode simulations determine the dimensions of the nested spherical resonator in Fig. 1 so that modes 2–4 resonate around the desired center frequency f_c.

2) Perform a set of parametric studies as shown in Fig. 10 to determine the passband BW, TZs, stopband isolation, and the filter matching levels.

3) Select r_p for the desired filter BW to be obtained.

4) Specify the location of the TZs by altering r_p (TZ_2) and r_1 (TZ_1, TZ_2, and TZ_3).

5) Adjust the stopband isolation by altering r_p and θ_2.

6) Through θ_2 specify the desired RL level.

D. Six-Pole BPF

To explore the scalability of the multimode resonator concept in Section II-C to higher order transfer functions, a filter geometry comprising two in-series cascaded multimode resonators (mode 2–4 contribute to the filter passband) and having a six-pole transfer function is considered next. The nested spherical cavity resonators are cascaded with an air-filled coaxial transmission line (TL) as shown in Fig. 11. Figs. 12–14 demonstrate how the transfer function characteristics of the six-pole BPF are controlled by altering its geometrical parameters. As shown in Fig. 12(a) and (b) the in-band RL, bandwidth, and stopband isolation at high frequency can be adjusted by controlling r_p and θ_3. Furthermore, as shown in Fig. 13, the in-band RL and stopband isolation

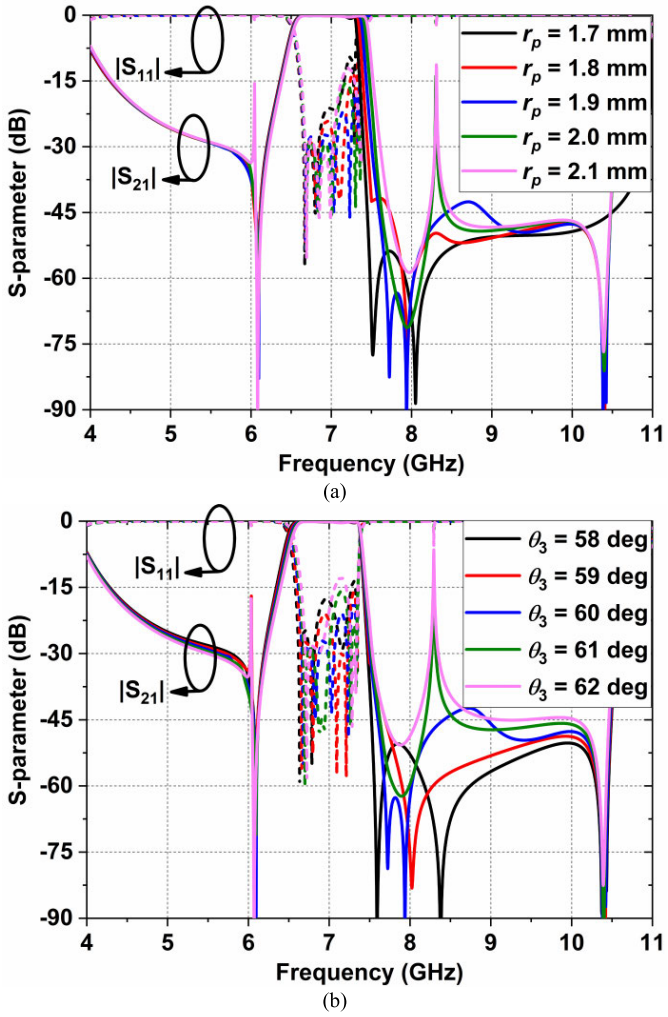

Fig. 12. EM-simulated S-parameters of the six-pole BPF in Fig. 11 as a function of alternative geometrical parameters. (a) r_p. (b) θ_3. In these results, $r_1 = 9.2$ mm, $r_2 = 13.9$ mm, $r_{t1} = 0.7$ mm, $r_{t2} = 1.8$ mm, and $c_l = 31.6$ mm.

at high frequency can be adjusted by altering the radius r_{t1} of the inner conductor of air-filled coaxial TL and the length c_l of air-filled coaxial TL affect the in-band RL and the out-of-band spur performance as shown in Fig. 14. Taking into consideration the aforementioned design trade-offs the six-pole BPF is designed as follows.

1) Determine the dimensions of the nested spherical resonator in Fig. 1 according to eigenmode simulations so that modes 2–4 of the resonator can resonate around the desired center frequency f_c.

2) Cascade two nested resonators with an air-filled coaxial TL as shown in Fig. 11 and perform a set of parametric studies as shown in Figs. 12–14 to determine stopband isolation and filter matching.

3) Select r_p for the desired filter BW to be obtained.

4) Adjust the stopband isolation by altering r_p, θ_3, r_{t1}, and c_l.

5) Through r_{t1} and θ_3 specify the desired RL level.

III. Experimental Results

To verify the practical viability of the nested spherical resonator-based BPF concept, three filter prototypes

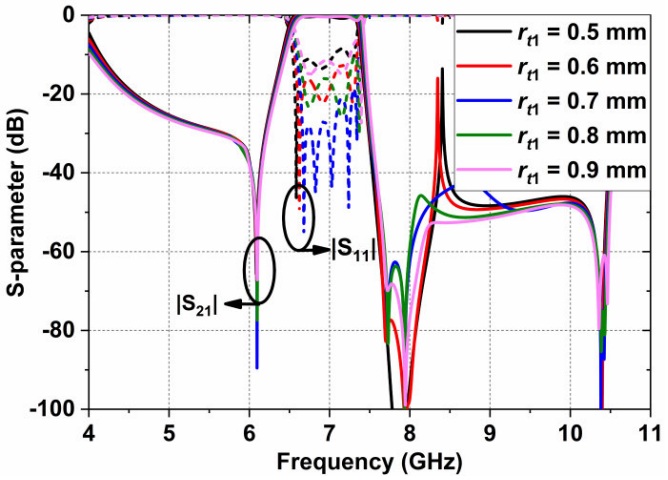

(a)

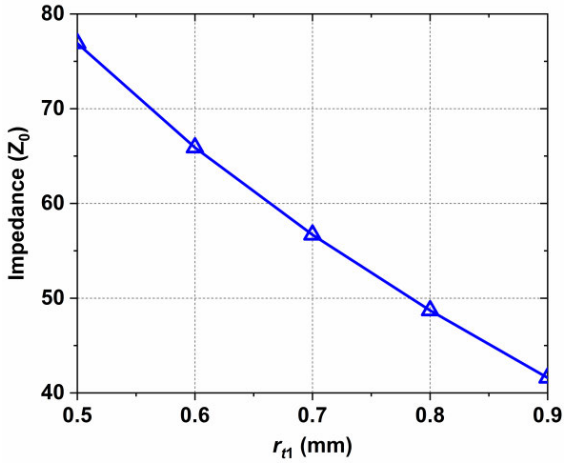

(b)

Fig. 13. (a) EM-simulated S-parameters of the six-pole BPF in Fig. 11 as a function of the radius r_{t1} of the inner conductor of the air-filled coaxial TL. (b) Characteristic impedance of the coaxial TL as a function of r_{t1}. The rest of the geometrical parameters are: $r_1 = 9.2$ mm, $r_2 = 13.9$ mm, $r_p = 1.91$ mm, $r_{t2} = 1.8$ mm, $c_l = 31.6$ mm, and $\theta_3 = 60°$.

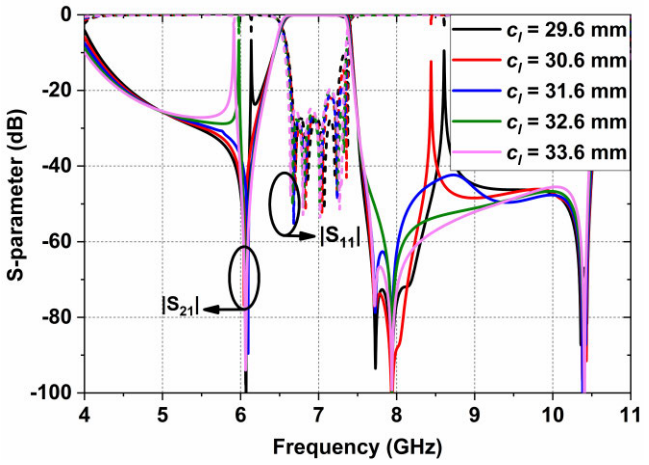

Fig. 14. EM-simulated S-parameters of the six-pole BPF as a function of the length c_l of the air-filled coaxial TL. In these results, $r_1 = 9.2$ mm, $r_2 = 13.9$ mm, $r_p = 1.91$ mm, $r_{t1} = 0.7$ mm, $r_{t2} = 1.8$ mm, and $\theta_3 = 60°$.

were designed, manufactured, and measured. All of the BPFs were manufactured monolithically using SLA 3-D printing

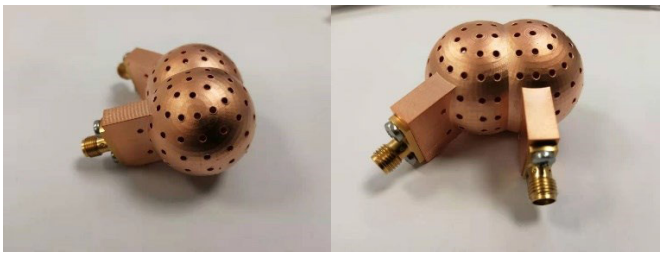

(a)

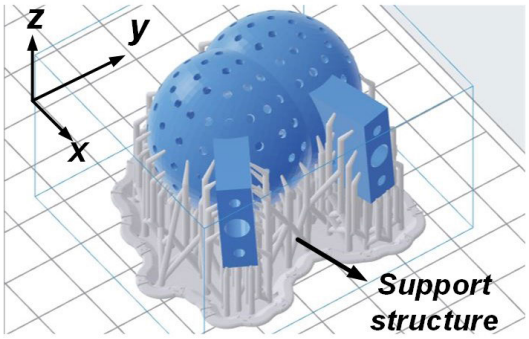

(b)

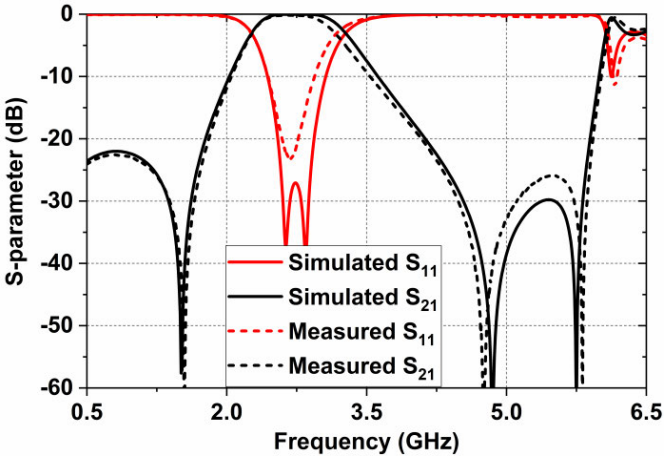

(c)

Fig. 15. Experimental validation of the two-pole BPF. (a) Manufactured prototype. (b) CAD model for SLA-based monolithic manufacturing. (c) Measured and simulated S-parameters. The dimensions of this filter are $r_1 = 7.1$ mm, $r_2 = 14$ mm, $r_p = 1.5$ mm, $g = 2$ mm, $r_c = 5.08$ mm, and $\theta_1 = 45°$.

with a 50 μm layer resolution. Metallization was performed using a commercially available platting process that creates a 50 μm Cu-layer across all surfaces.

A. Two-Pole BPF

The manufactured prototype of two-pole BPF is shown in Fig. 15(a) and its corresponding CAD model for SLA monolithic 3-D printing is provided in Fig. 15(b). The RF measured response of the two-pole BPF is depicted in Fig. 15(c) and is summarized as follows: center frequency f_c of 2.72 GHz and the 3-dB FBW of 33.1%. The measured minimum IL was measured around 0.15 and the passband RL around 23.2 dB. A comparison with the EM simulated response is also included and appears to be in good agreement successfully validating the proposed filter concept.

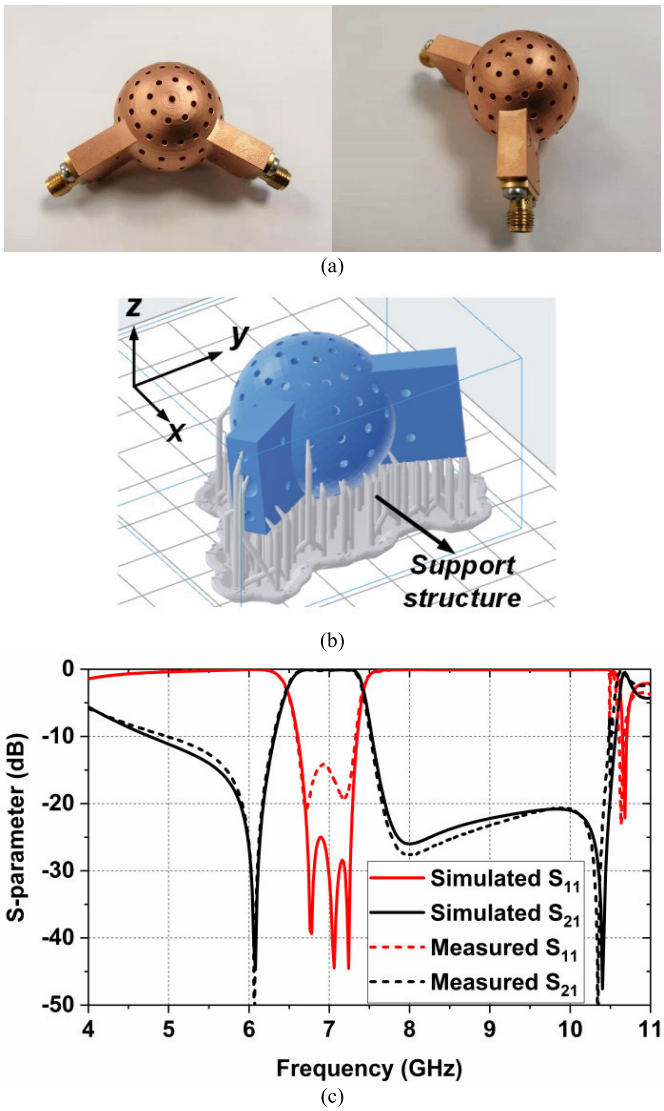

Fig. 16. Experimental validation of the three-poles BPF. (a) Manufactured prototype. (b) CAD model for SLA-based monolithic manufacturing. (c) RF-measured and EM-simulated S-parameters. The dimensions of this filter are $r_1 = 9.1$ mm, $r_2 = 14$ mm, $r_p = 1.9$ mm, and $\theta_2 = 62°$.

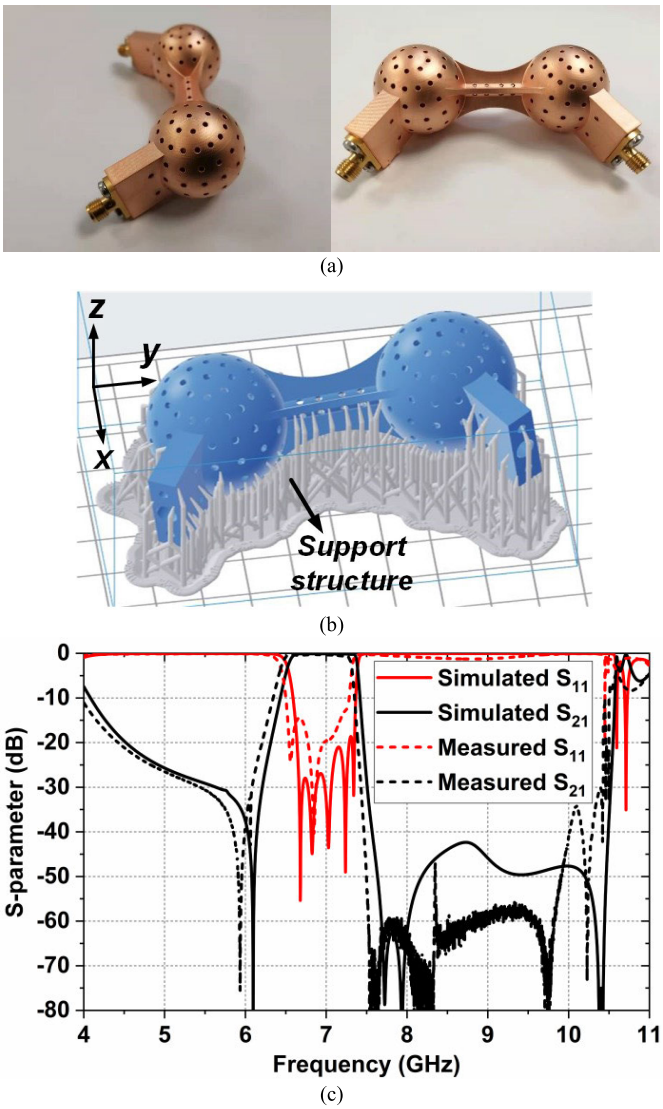

Fig. 17. Experimental validation of six-poles BPF. (a) Prototype after copper plating in different perspectives. (b) CAD model for SLA-based monolithic manufacturing. (c) Measured and simulated S-parameters. The dimensions of this filter are $r_1 = 9.2$ mm, $r_2 = 13.9$ mm, $r_p = 1.91$ mm, $r_{t1} = 0.7$ mm, $r_{t2} = 1.8$ mm, $c_l = 31.6$ mm, and $\theta_3 = 60°$.

B. Three-Pole BPF

The manufactured prototype and CAD model of SLA manufacturing of three-pole BPF is shown in Fig. 16(a) and (b) respectively. The measured S-parameters are shown in Fig. 16(c) and its RF measured performance is summarized as follows: f_c: 6.94 GHz, 3-dB FBW 13.65%, minimum in-band IL of 0.07 dB, and passband RL is better than 14.2 dB. A comparison with its corresponding EM simulated response is also provided in the same figure and appears to be in good agreement with the RF measured response.

C. Six-Pole BPF

The experimental validation of the six-pole BPF concept has been performed through the manufacturing and testing of the prototype in Fig. 17(a). Its corresponding CAD model for SLA manufacturing is shown in Fig. 17(b) and the measured S-parameters are shown in Fig. 17(c). Its RF measured performance is summarized as follows: f_c: 6.88 GHz, 3-dB FBW 12.77%, minimum IL of 0.3 dB, and passband RL is better than 12.6 dB.

D. Comparison With the State of the Art

Table I shows a comparison of the proposed nested spherical BPF concept with state-of-the-art 3-D printed 3-D BPFs using traditional hollow spherical, waveguide, coaxial, and 3-D resonators with irregular shapes. As shown, the proposed filter concept has a smaller size than all the filters based on traditional hollow spherical resonators and exhibits lower IL. Furthermore, the proposed concept has been demonstrated for higher order transfer functions and is the only BPF concept based on nested spherical resonators that are reported in this work for the first time.

TABLE I
COMPARISON WITH STATE OF THE ART 3-D PRINTED FILTERS

Ref.	Tech.	R.T.	Order	f_c (GHz)	IL (dB)	FBW (%)	Size (λ_0^3)
[10]	SLA/Mo.	Coaxial	4	3.5	0.45	9.6	1.01×0.76×N/A
[24]	SLA/S.B.	Irregular	4	1.8	0.54	4.5	0.42×0.138×0.15
[42]	SLA/Mo.	Spherical	4	34.8	1.7	5.7	N/A
[43]	SLM/Mo.	Spherical	3	10	0.33	1	3.5×1.33×1.33
[48]	SLA/S.B.	Spherical	5	10	0.11	5	4×1.7×1.67
[49]	SLA/ Mo.	Spherical	4	10	0.25	3	2.53×1×1.03
[50]	SLM/Mo.	Spherical	4	31	1.53	2.84	6.3×1.96×1.96
This work	SLA/Mo.	N.S.	2	2.72	0.15	33.1	0.42×0.36×0.27
This work	SLA/Mo.	N.S.	3	6.94	0.07	13.65	0.97×0.92×0.69
This work	SLA/Mo.	N.S.	6	6.88	0.3	12.77	1.88×0.91×0.69

(Ref: reference, S.B.: split-block, Mo.: monolithic, R.T.: resonator type, N.S.: nested spherical, N/A: not available.)

IV. CONCLUSION

New types of highly miniaturized spherical resonator-based BPFs were presented. They are based on nested spherical resonators whose resonant frequencies are lowered by incorporating a postsupported sphere. Miniaturized prototypes using the fundamental mode as well as a combination of higher order modes are demonstrated for the first time. A compact monolithic integration scheme using SLA 3-D printing is also proposed for size compactness and low weight when compared to conventional split-block integration schemes. Multiple BPF prototypes using the fundamental mode as well as a combination of three higher order modes were designed, manufactured, and tested at *S*-band and *C*-band.

REFERENCES

[1] Q. Wu, F. Zhu, Y. Yang, and X. Shi, "An effective approach to suppressing the spurious mode in rectangular waveguide filters," *IEEE Microw. Wireless Compon. Lett.*, vol. 29, no. 11, pp. 703–705, Nov. 2019.

[2] P. Zhao and K. Wu, "Waveguide filters with central-post resonators," *IEEE Microw. Wireless Compon. Lett.*, vol. 30, no. 7, pp. 657–660, Jul. 2020.

[3] B. Gowrish, S. K. Koul, and R. R. Mansour, "Transversal coupled triple-mode spherical resonator-based bandpass filters," *IEEE Microw. Wireless Compon. Lett.*, vol. 31, no. 4, pp. 369–372, Apr. 2021.

[4] A. Morini et al., "Modeling and design of microwave filters employing overmoded empty cylindrical resonators," in *Proc. Eur. Microw. Conf. (EuMC)*, Sep. 2015, pp. 971–974.

[5] L.-X. Zeng and F.-M. Lin, "Miniaturized high-performance cube-shaped filter made up of quasi-TM_{010} mode dielectric-loaded cavities," *IEEE Access*, vol. 8, pp. 847–855, 2020.

[6] U. Rosenberg, R. Beyer, P. Krauß, T. Sieverding, P. M. Iglesias, and C. Ernst, "Remote controlled high-Q cavity filters providing center frequency and bandwidth re-allocation," in *IEEE MTT-S Int. Microw. Symp. Dig.*, Sep. 2017, pp. 1–3.

[7] B. Yassini and M. Yu, "A novel Ka band dual mode super Q cavity filter," in *IEEE MTT-S Int. Microw. Symp. Dig.*, Jun. 2014, pp. 1–3, doi: 10.1109/MWSYM.2014.6848452.

[8] O. A. Peverini et al., "Enhanced topology of *E*-plane resonators for high-power satellite applications," *IEEE Trans. Microw. Theory Techn.*, vol. 63, no. 10, pp. 3361–3373, Oct. 2015.

[9] K. Zhao and D. Psychogiou, "A monolithic vertical integration concept for compact coaxial-resonator-based bandpass filters using additive manufacturing," *IEEE Microw. Wireless Compon. Lett.*, vol. 31, no. 6, pp. 689–692, Jun. 2021.

[10] K. Zhao and D. Psychogiou, "Spurious suppression techniques for 3-D printed coaxial resonator bandpass filters," *IEEE Microw. Wireless Compon. Lett.*, vol. 32, no. 1, pp. 33–36, Jan. 2022.

[11] J. A. Ruiz-Cruz, M. A. E. Sabbagh, K. A. Zaki, J. M. Rebollar, and Y. Zhang, "Canonical ridge waveguide filters in LTCC or metallic resonators," *IEEE Trans. Microw. Theory Techn.*, vol. 53, no. 1, pp. 174–182, Jan. 2005.

[12] A. Kirilenko, L. Rud, V. Tkachenko, and D. Kulik, "Evanescent-mode ridged waveguide bandpass filters with improved performance," *IEEE Trans. Microw. Theory Techn.*, vol. 50, no. 5, pp. 1324–1327, May 2002.

[13] S. Bastioli, C. Tomassoni, and R. Sorrentino, "A new class of waveguide dual-mode filters using TM and nonresonating modes," *IEEE Trans. Microw. Theory Techn.*, vol. 58, no. 12, pp. 3909–3917, Dec. 2010.

[14] T. Qin, X. Q. Lin, and Y. L. Fan, "Analysis, design, and implementation of miniaturized multimode waveguide filters based on epsilon-near-zero channel concept," *IEEE Trans. Microw. Theory Techn.*, vol. 69, no. 8, pp. 3598–3606, Aug. 2021.

[15] D. R. Hendry and A. M. Abbosh, "Parallel multimode cavity filters with generalized frequency response," *IEEE Trans. Microw. Theory Techn.*, vol. 67, no. 5, pp. 1844–1853, May 2019.

[16] G. Basavarajappa and R. R. Mansour, "A high-*Q* quadruple-mode rectangular waveguide resonator," *IEEE Microw. Wireless Compon. Lett.*, vol. 29, no. 5, pp. 324–326, May 2019.

[17] M. D'Auria et al., "3-D printed metal-pipe rectangular waveguides," *IEEE Trans. Compon., Packag., Manuf. Technol.*, vol. 5, no. 9, pp. 1339–1349, Sep. 2015.

[18] J. Shen and D. S. Ricketts, "Additive manufacturing of complex millimeter-wave waveguides structures using digital light processing," *IEEE Trans. Microw. Theory Techn.*, vol. 67, no. 3, pp. 883–895, Mar. 2019.

[19] T.-H. Chio, G.-L. Huang, and S.-G. Zhou, "Application of direct metal laser sintering to waveguide-based passive microwave components, antennas, and antenna arrays," *Proc. IEEE*, vol. 105, no. 4, pp. 632–644, Apr. 2017.

[20] B. Zhang and H. Zirath, "A metallic 3-D printed E-band radio front end," *IEEE Microw. Wireless Compon. Lett.*, vol. 26, no. 5, pp. 331–333, May 2016.

[21] C. R. Garcia, R. C. Rumpf, H. H. Tsang, and J. H. Barton, "Effects of extreme surface roughness on 3D printed horn antenna," *Electron. Lett.*, vol. 49, no. 12, pp. 734–736, Jun. 2013.

[22] Y. Chen et al., "3-D printed dual-band filter based on spherical dual-mode cavity," *IEEE Microw. Wireless Compon. Lett.*, vol. 31, no. 9, pp. 1047–1050, Sep. 2021.

[23] A. Vallecchi, D. Cadman, W. G. Whittow, J. Vardaxoglou, E. Shamonina, and C. J. Stevens, "3-D printed bandpass filters with coupled vertically extruded split ring resonators," *IEEE Trans. Microw. Theory Techn.*, vol. 67, no. 11, pp. 4341–4352, Nov. 2019.

[24] G. Venanzoni, M. Dionigi, C. Tomassoni, and R. Sorrentino, "3-D-printed quasi-elliptical evanescent mode filter using mixed electromagnetic coupling," *IEEE Microw. Wireless Compon. Lett.*, vol. 28, no. 6, pp. 497–499, Jun. 2018.

[25] K. Zhao and D. Psychogiou, "Monolithic multiband coaxial resonator-based bandpass filter using stereolithography apparatus (SLA) manufacturing," *IEEE Trans. Microw. Theory Techn.*, vol. 70, no. 9, pp. 4156–4166, Sep. 2022.

[26] M. Salek, X. Shang, and M. J. Lancaster, "Compact *S*-band coaxial cavity resonator filter fabricated by 3-D printing," *IEEE Microw. Wireless Compon. Lett.*, vol. 29, no. 6, pp. 382–384, Jun. 2019.

[27] R. Dahle, P. Laforge, and J. Kuhling, "3-D printed customizable inserts for waveguide filter design at X-band," *IEEE Microw. Wireless Compon. Lett.*, vol. 27, no. 12, pp. 1080–1082, Dec. 2017.

[28] M. Mirmozafari, S. Saeedi, H. Saeidi-Manesh, G. Zhang, and H. H. Sigmarsson, "Direct 3-D printing of nonplanar linear-dipole-phased array antennas," *IEEE Antennas Wireless Propag. Lett.*, vol. 17, no. 11, pp. 2137–2140, Nov. 2018.

[29] M. F. Farooqui and A. Kishk, "3-D-Printed tunable circularly polarized microstrip patch antenna," *IEEE Antennas Wireless Propag. Lett.*, vol. 18, no. 7, pp. 1429–1432, Jul. 2019.

[30] Y. Li et al., "3-D printed high-gain wideband waveguide fed horn antenna arrays for millimeter-wave applications," *IEEE Trans. Antennas Propag.*, vol. 67, no. 5, pp. 2868–2877, May 2019.

[31] I. Agnihotri and S. K. Sharma, "Design of a 3D metal printed axial corrugated horn antenna covering full Ka-band," *IEEE Antennas Wireless Propag. Lett.*, vol. 19, no. 4, pp. 522–526, Apr. 2020.

[32] K. Lomakin et al., "3D printed E-band hybrid coupler," *IEEE Microw. Wireless Compon. Lett.*, vol. 29, no. 9, pp. 580–582, Sep. 2019.

[33] J. Sorocki, I. Piekarz, S. Gruszczynski, K. Wincza, and J. Papapolymerou, "Application of 3-D printing technology for the realization of high-performance directional couplers in suspended stripline technique," *IEEE Trans. Compon., Packag., Manuf. Technol.*, vol. 9, no. 8, pp. 1652–1658, Aug. 2019.

[34] W. Liu, Z. Chen, T. Viola, and G. H. Huff, "3-D printed directional couplers in circular waveguide," *IEEE Microw. Wireless Compon. Lett.*, vol. 31, no. 6, pp. 561–564, Jun. 2021.

[35] D. Bruhn et al., "Effects of cutting planes on filter performance of FDM 3D-printed X-band waveguide filters," in *IEEE MTT-S Int. Microw. Symp. Dig.*, Nov. 2021, pp. 236–238.

[36] D. Miek, S. Simmich, F. Kamrath, and M. Höft, "Additive manufacturing of E-plane cut dual-mode X-band waveguide filters with mixed topologies," *IEEE Trans. Microw. Theory Techn.*, vol. 68, no. 6, pp. 2097–2107, Jun. 2020.

[37] C. Tomassoni, G. Venanzoni, M. Dionigi, and R. Sorrentino, "Compact quasi-elliptic filters with mushroom-shaped resonators manufactured with 3-D printer," *IEEE Trans. Microw. Theory Techn.*, vol. 66, no. 8, pp. 3579–3588, Aug. 2018.

[38] C. Guo et al., "Monolithic 3D printed waveguide filters with wide spurious-free stopbands using dimpled spherical resonators," *IET Microw., Antennas Propag.*, vol. 15, no. 12, pp. 1657–1670, Oct. 2021.

[39] J. Li, K.-D. Hong, and T. Yuan, "Slotted hemispherical resonators for 3-D printed waveguide filters with extended spurious-free stopbands," *IEEE Access*, vol. 7, pp. 130221–130235, 2019.

[40] X. Wen et al., "SLM printed waveguide dual-mode filters with reduced sensitivity to fabrication imperfections," *IEEE Microw. Wireless Compon. Lett.*, vol. 31, no. 11, pp. 1195–1198, Nov. 2021.

[41] J. Li, C. Guo, J. Xu, and L. Mao, "Lightweight low-cost Ka-band 3-D printed slotted rectangular waveguide bandpass filters," in *Proc. IEEE Int. Symp. Antennas Propag. USNC/URSI Nat. Radio Sci. Meeting*, Jul. 2017, pp. 2647–2648.

[42] Y. Li, J. Li, M. Zhang, H. Wang, J. Xu, and S. Xiao, "A monolithic stereolithography 3-D printed Ka-band spherical resonator bandpass filter," in *Proc. IEEE Radio Wireless Symp. (RWS)*, Jan. 2018, pp. 56–59.

[43] F. Zhang et al., "3-D printed slotted spherical resonator bandpass filters with spurious suppression," *IEEE Access*, vol. 7, pp. 128026–128034, 2019.

[44] J. Li, G. Huang, and T. Yuan, "Monolithic 3-D printed spherical-resonator-based olympic-topology bandpass filters," in *Proc. IEEE Int. Symp. Antennas Propag. USNC/URSI Nat. Radio Sci. Meeting*, Jul. 2018, pp. 1441–1442.

[45] K. Zhao and D. Psychogiou, "Monolithically-integrated 3D printed coaxial bandpass filters and RF diplexers: Single-band and dual-band," *Int. J. Microw. Wireless Technol.*, vol. 14, no. 3, pp. 293–304, Apr. 2022.

[46] G. Venanzoni, C. Tomassoni, M. Dionigi, M. Mongiardo, and R. Sorrentino, "Design and fabrication of 3-D printed inline coaxial filters with improved stopband," *IEEE Trans. Microw. Theory Techn.*, vol. 68, no. 7, pp. 2633–2643, Jul. 2020.

[47] E. López-Oliver et al., "3-D-Printed compact bandpass filters based on conical posts," *IEEE Trans. Microw. Theory Techn.*, vol. 69, no. 1, pp. 616–628, Jan. 2021.

[48] C. Guo, X. Shang, M. J. Lancaster, and J. Xu, "A 3-D printed lightweight X-band waveguide filter based on spherical resonators," *IEEE Microw. Wireless Compon. Lett.*, vol. 25, no. 7, pp. 442–444, Jul. 2015.

[49] C. Guo, X. Shang, J. Li, F. Zhang, M. J. Lancaster, and J. Xu, "A lightweight 3-D printed *X*-band bandpass filter based on spherical dual-mode resonators," *IEEE Microw. Wireless Compon. Lett.*, vol. 26, no. 8, pp. 568–570, Aug. 2016.

[50] F. Zhang et al., "A 3-D printed bandpass filter using TM_{211}-mode slotted spherical resonators with enhanced spurious suppression," *IEEE Access*, vol. 8, pp. 213215–213223, 2020.

Jiawei Liu (Member, IEEE) received the bachelor's degree in electrical engineering from Southwest Minzu University, Chengdu, China, in 2017. He is currently pursuing the Ph.D. degree in electrical engineering with the University of Electronic Science and Technology of China (UESTC), Chengdu.

His main research interests include RF/microwave and mm-wave circuits and systems.

Kunchen Zhao (Graduate Student Member, IEEE) received the bachelor's degree in electrical engineering from the University of Electronic Science and Technology of China, Chengdu, China, in 2018, and the master's degree in electrical engineering from The Ohio State University, Columbus, OH, USA, in 2019. He is currently pursuing the Ph.D. degree in RF/microwave engineering with the University of Colorado Boulder, Boulder, CO, USA.

His main research interests include the design of high performance RF passive circuits.

Dimitra Psychogiou (Senior Member, IEEE) received the Dipl.Eng. degree in electrical and computer engineering from the University of Patras, Patras, Greece, in 2008, and the Ph.D. degree in electrical engineering from the Swiss Federal Institute of Technology (ETH), Zürich, Switzerland, in 2013.

She is currently a Professor of electrical and electronic engineering with the University College Cork (UCC), Cork, Ireland, and the Head of the Advanced RF Technology Group, Tyndall National Institute, Cork. Prior to joining UCC, she was a Senior Research Scientist with Purdue University, West Lafayette, IN, USA, and an Assistant Professor with the University of Colorado Boulder (UC Boulder), Boulder, CO, USA. Her current research interests include RF design and characterization of reconfigurable microwave and millimeter-wave passive components, RF-MEMS, acoustic wave resonator-based filters, tunable filter synthesis, frequency-agile antennas, and additive manufacturing (AM) technologies for 3-D antenna subsystems.

Dr. Psychogiou is a Senior Member of the International Union of Radio Science (URSI) and a member of the IEEE MTT-S Filters and Passive Components (MTT-5) and Microwave Control Materials and Devices (MTT-13) committees. She serves on the Technical Review Board for various IEEE and EuMA conferences and journals. She research has received the 2021 Roberto Sorrentino Prize, the SFI Research Professorship Award, the 2020 NSF CAREER Award, the 2020 URSI Young Scientist Award, and the Junior Faculty Outstanding Research Award from UC Boulder. She is the Chair of MMT-13 and the Secretary of USNC-URSI Commission D. She is an Associate Editor of the IEEE MICROWAVE AND WIRELESS COMPONENTS LETTERS and the *International Journal of Microwave and Wireless Technologies*. She was an Associate Editor of the *IET Microwaves, Antennas and Propagation*journal.